PHYSICAL REVIEW B **91**, 075126 (2015)

Structural, electronic, and spectral properties of six ZnO bulk polymorphs

Lorenzo Sponza,[*] Jacek Goniakowski, and Claudine Noguera
CNRS, UMR 7588, Institut des Nanosciences de Paris, F-75005 Paris, France
and Sorbonne Universités, UPMC Université Paris 06, UMR 7588, INSP, F-75005 Paris, France

(Received 27 November 2014; revised manuscript received 26 January 2015; published 23 February 2015)

Relying on HSE03, G_0W_0, and random phase approximation + G_0W_0 approaches, this study provides a complete characterization of the electronic properties of six ZnO bulk polymorphs, including quasiparticle spectra, absorption, and electron energy-loss spectra. It focuses on the series zinc blende, wurtzite, body-centered tetragonal, sodalite, and cubane structures, along which atoms have similar local tetrahedral environments and decreasing atomic density, to which the hexagonal boron nitride structure was added. All trends in the electronic properties—gap opening, blueshift of low-energy interband transitions, redshift of the main absorption peak, the frequency at which the real part of the dielectric tensor vanishes, and the plasmon energy—were interpreted in terms of the two main effects resulting from the decrease of the atomic density along the series: a bandwidth narrowing close to the gap edge and a decrease (in absolute value) of the electrostatic potential acting on the zinc and oxygen ions. This work gives firm grounds to help and foster spectroscopic experiments on ZnO polymorphs. It represents a preliminary step towards the study of thin-film properties.

DOI: 10.1103/PhysRevB.91.075126 PACS number(s): 71.20.Nr, 78.20.Bh, 78.40.Fy

I. INTRODUCTION

Zinc oxide (ZnO) is a wide-gap semiconductor [1] which crystallizes in the wurtzite structure under normal conditions. Due to its peculiar optoelectronic properties, it has been used to benchmark novel theoretical or computational approaches [2–8] as well as employed in many technological applications, such as transparent electronics, field emitters, gas sensors, or solar cells [9–11].

Besides the wurtzite polymorph, diverse bulk structures have been predicted to be stable under suitable thermodynamic conditions [12–16], and some of them have been synthesized [17–21]. Similarly, a wide variety of ZnO nanostructures can be produced [22]. In particular, an active field of research with potential fruitful technological applications focuses on ultrathin films [23–26] whose properties, especially the electronic ones, are still lacking full theoretical and experimental characterization.

In this context, the possibility of tuning electronic and optical properties through structural modifications calls for a more thorough understanding of the properties of ZnO bulk polymorphs. In recent years, various authors have compared the electronic structure of wurtzite and zinc blende to those of the rocksalt and cesium chloride polymorphs [4,12,27,28], but the latter materials are stable only under high pressure.

On the other hand, most recent work on other ZnO polymorphs—hexagonal boron nitride, body-centered tetragonal sodalite and cubane—focuses only on stability curves or critical pressures for structural phase transitions [13,29], with no detailed analysis of the electronic structure and excited-state properties. Only very recently have their gap widths been scrutinized [30,31].

The present theoretical work aims at a full characterization of quasiparticle (QP), absorption, and electron energy-loss (EELS) spectra of representative ambient-pressure ZnO polymorphs to help the interpretation of spectroscopic experiments. We have chosen to focus on the following series: zinc blende, wurtzite, body-centered tetragonal (bct), sodalite, and cubane structures, along which atoms have similar local tetrahedral environments and decreasing atomic density. We have added the hexagonal boron nitride structure (*h*-BN) in view of its importance in ultrathin films.

The paper is organized as follows: In Sec. II, after details of the computational setup, the structural properties of the six polymorphs are presented and discussed. Section III is devoted to the characterization of the QP spectra and band gaps. The absorption and the electron energy-loss spectra of the six polymorphs are the subject of Sec. IV, with a focus on their most notable peaks and a comparison with the QP structures highlighted in the previous section. Section V gives a summary of the main results of the study and conclusions.

II. STRUCTURAL PROPERTIES

As a preliminary step to their electronic properties, this section focuses on the ground-state characteristics of six ZnO polymorphs (wurtzite, zinc blende, *h*-BN, bct, sodalite, and cubane). Two exchange-correlation (XC) potentials and two pseudopotentials are used to predict equilibrium structures, cohesive energies, and bulk moduli. The wurtzite structure serves as a benchmark to validate the method to be applied to other polymorphs for which no experimental data are available.

A. Computational details

All ground-state calculations are performed within the framework of the density functional theory, using the projector-augmented wave (PAW) method [32,33], and a plane-wave basis set, as implemented in VASP [34]. Oxygen atoms participate in the valence band with six electrons each, whereas two Zn pseudopotentials (labeled Zn^{12+} and Zn^{20+}) have been tested, according to whether $3d^{10}4s^2$ or $3s^23p^63d^{10}4s^2$ electrons are kept in the valence, respectively. The Perdew-Burke-Ernzerhof (PBE) generalized-gradient

---

[*] Present address: King's College London, Strand campus, London WC2R 2LS, England, United Kingdom.

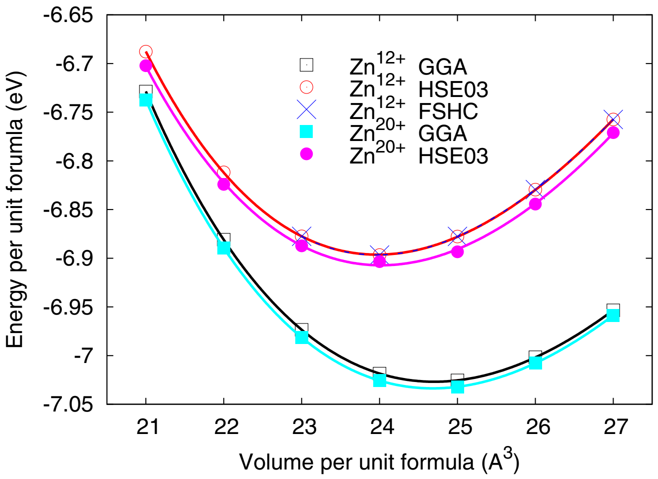

FIG. 1. (Color online) Wurtzite energy versus volume $E(V)$ curves, computed with PBE (generalised gradient approximation GGA) and HSE03 XC functionals and the FSHC scheme (see text), in which the core electrons are represented by the Zn^{12+} or Zn^{20+} pseudopotential.

approximation [35] is used, in parallel with the range-separated hybrid Heyd-Scuseria-Ernzerhof (HSE03) XC functional [36].

A cutoff energy of 600 eV is used for all polymorphs, in both PBE and HSE03 calculations. The k-point meshes used to sample the Brillouin zone are $8 \times 8 \times 8$ for zinc blende, $8 \times 8 \times 6$ for wurtzite and h-BN structures, $6 \times 6 \times 6$ for the sodalite structure, $4 \times 4 \times 6$ for the bct structure, and $4 \times 4 \times 4$ for cubane. All atomic degrees of freedom are relaxed until the maximum forces get smaller than 0.01 eV/Å and until all components of the stress tensor are lower than 0.01 eV/Å^3. These settings lead to converged values of the cell parameter within 0.01 Å and of the cohesive energy within 0.01 eV per formula unit. Only the ideal bct structure ($a = b$) has been considered.

B. Benchmarking the method on the wurtzite polymorph

In the PBE and HSE03 schemes, the wurtzite formation energy per formula unit $E(V)$ with respect to isolated atoms is first computed at fixed volumes V, after full cell shape and internal parameter u optimization. It is then fitted with a Birch-Murnaghan equation of state [37], which gives the cohesive energy, the equilibrium volume, and the bulk modulus.

The PBE and HSE03 $E(V)$ curves, obtained with the Zn^{12+} and Zn^{20+} pseudopotentials, are presented in Fig. 1, and the related structural parameters (a, c/a, u), bulk moduli K, cohesive energies E_c, and gaps E_g [computed from the energy difference between the top of the valence band (VB) and the bottom of the conduction band (CB)] are reported in Table I together with experimental data [1,38–41].

The two pseudopotentials give nearly indistinguishable results, not only on structural properties, but also for the prediction of gap widths (Table I), in good agreement with similar theoretical calculations [4,31,42]. As a consequence, the less computationally demanding Zn^{12+} pseudopotential will be adequate for the simulation of other polymorphs. The HSE03 potential leads to smaller equilibrium cells, but the c/a ratio and the u parameter do not change with respect to their PBE values. In HSE03, the d electrons of Zn are more localized than in the PBE scheme, which results in a higher screening of the ionic charges. This allows ions to get closer to each other (volume reduction) without modifying the bond angles.

In passing, considering the HSE03 computation cost, we have tested a less demanding but approximate optimization method. It consists of the calculation of the $E(V)$ curve including structural optimization at the PBE level, followed by a mere HSE03 electronic structure calculation for each V value. This fixed-structure hybrid correction (FSHC) to the PBE energy depends on the atomic arrangement, which means that the corresponding $E^{\mathrm{FSHC}}(V)$ curve is not a simple shift of $E^{\mathrm{PBE}}(V)$. Its results for ZnO bulk wurtzite are reported in Fig. 1 and Table I. With a much lower computational cost, the FSHC method performs as well as full HSE03 optimization.

C. Structural properties of ZnO polymorphs

The six ZnO polymorphs under consideration display various atomic densities and local atomic arrangements (Fig. 2), which are reflected in their relative stability and electronic properties. The zinc blende, wurtzite, ideal bct, sodalite, and cubane phases are characterized by similar local geometries, with Zn atoms in a tetrahedral environment (number of first neighbors $N_1 = 4$; Table II). The tetrahedra are almost ideal in zinc blende and wurtzite, but distorted in other structures, with slight variations in angles but almost similar average bond lengths. They are arranged differently in the different structures, leading to different second-neighbor numbers N_2, ranging from 12 (wurtzite, zinc blende, h-BN phases) to 9 in the least dense cubane phase. In the following, we will analyze structural and electronic trends along the series zinc blende, wurtzite, bct, sodalite, and cubane, along which N_2 decreases. The h-BN polymorph represents an exception, as

TABLE I. Ground-state properties of ZnO wurtzite: lattice parameter a (Å), ratio c/a, internal parameter u, bulk modulus K (GPa), cohesive energy with respect to atoms E_c (eV/ formula unit), and gap width E_g (eV).

		a (Å)	c/a	u	K (GPa)	E_c (eV)	E_g (eV)
Zn^{12+}	PBE	3.28	1.61	0.38	128.5	7.03	0.73
	HSE03	3.25	1.61	0.38	142.9	6.90	2.27
	FSHC	3.25	1.61	0.38	145.8	6.90	2.27
Zn^{20+}	PBE	3.28	1.61	0.38	129.0	7.03	0.74
	HSE03	3.25	1.61	0.38	140.1	6.90	2.29
Experiment		3.25 [38,39]	1.60 [38,39]	0.38–0.39 [38,40]	135–183 [38–40]	7.52 [41]	3.34 [1]

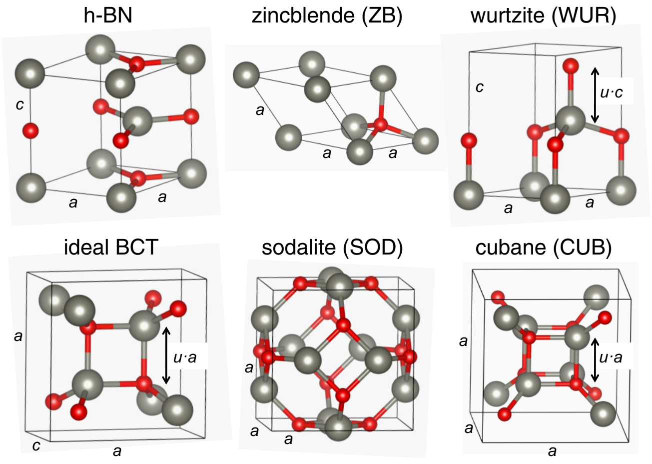

FIG. 2. (Color online) Primitive cells of the six ZnO polymorphs. Small (red) balls are O atoms, big (gray) ones are Zn.

far as first-neighbor coordination is concerned ($N_1 = 5$), since all its atoms have a trigonal bipyramidal environment.

Relying on PBE and HSE03 exchange-correlation functionals and making use of the Zn^{12+} pseudopotential, the $E(V)$ curves of the six polymorphs are reported in Fig. 3 and their structural characteristics in Table II. These results compare well with findings from other authors [4,12,13,29,31,42]. As for the case of wurtzite, the PBE calculation predicts larger cell parameters for all structures, although bonding angles are the same in HSE03 and PBE approximations. Cohesive energies are also larger in the PBE calculations (of the order of 0.10–0.15 eV) but the relative stability of the six polymorphs is identical in both approximations. Table II evidences an expected decrease of cohesion energy as the atomic density of the polymorphs becomes lower.

III. QUASIPARTICLE SPECTRA AND BAND GAPS

After a preliminary part devoted to a presentation of the computational approach and its application to the wurtzite phase, the PBE, HSE03, and G_0W_0 band gaps and quasiparticle spectra of the six ZnO polymorphs under consideration are analyzed, with a particular focus on the orbital character of the main peaks in the VB and CB.

A. Computational approach

Among known problems of local and semilocal density functional approaches, such as the PBE approximation, are the underestimation of the band gap in semiconductors and insulators and the excessive delocalization of d and f electrons. The HSE03 XC potential is meant to partially cure both problems. It coincides with the PBE XC potential, except at short distance from the nuclei, where the nonlocal exchange term is treated explicitly. On top of this, the G_0W_0 approach [43,44] adds dynamical screening (based on long-range Coulomb interaction) to the bare exchange terms. Hence, in view of discussing how electronic properties are affected by structural modifications at short and long distances, a comparison of the three approaches (PBE, HSE03, and G_0W_0) is relevant. The PBE and HSE03 calculations are performed with the same cutoff energy of 600 eV as previously. The quasiparticle corrections to the HSE03 energies are computed in the G_0W_0 scheme as implemented in VASP [45]. The GW gap of wurtzite ZnO has been computed to benchmark all-electron [3,46,47], or PAW [45,48] approaches, or to test performances in conjunction with refined starting points, as given by hybrid functionals [6,49]. It has been pointed out how fundamental and technical aspects may impact the results

TABLE II. Structural properties of the six ZnO polymorphs: lattice parameters a, b, and c (Å), internal parameter u, and average Zn-O distance $d_{\mathrm{Zn-O}}$(Å) together with bulk modulus K (GPa) and cohesive energy with respect to atoms E_c (eV/formula unit). N_1 and N_2 are the numbers of first and second neighbors, respectively

		PBE	HSE03
h-BN ($N_1 = 5$, $N_2 = 12$)			
	$a = b$	3.45	3.43
	c	4.60	4.50
	$d_{\mathrm{Zn-O}}$	2.11	2.09
	K	110.4	122.0
	E_c	6.88	6.76
Zinc blende ($N_1 = 4$, $N_2 = 12$)			
	$a = b = c$	3.27	3.24
	$d_{\mathrm{Zn-O}}$	2.00	1.98
	K	127.8	141.7
	E_c	7.01	6.87
Wurtzite ($N_1 = 4$, $N_2 = 12$)			
	$a = b$	3.28	3.25
	c	5.30	5.24
	u	0.38	0.38
	$d_{\mathrm{Zn-O}}$	2.00	1.98
	K	128.5	142.9
	E_c	7.03	6.90
Ideal bct ($N_1 = 4$, $N_2 = 11$)			
	$a = b$	5.62	5.55
	c	3.28	3.25
	u	0.36	0.36
	$d_{\mathrm{Zn-O}}$	2.00	1.98
	K	115.0	129.1
	E_c	6.98	6.85
Sodalite ($N_1 = 4$, $N_2 = 10$)			
	$a = b = c$	5.66	5.61
	$d_{\mathrm{Zn-O}}$	2.00	1.98
	K	104.3	115.1
	E_c	6.90	6.76
Cubane ($N_1 = 4$, $N_2 = 9$)			
	$a = b = c$	6.28	6.22
	u	0.33	0.33
	$d_{\mathrm{Zn-O}}$	2.01	1.99
	K	99.8	110.9
	E_c	6.81	6.66

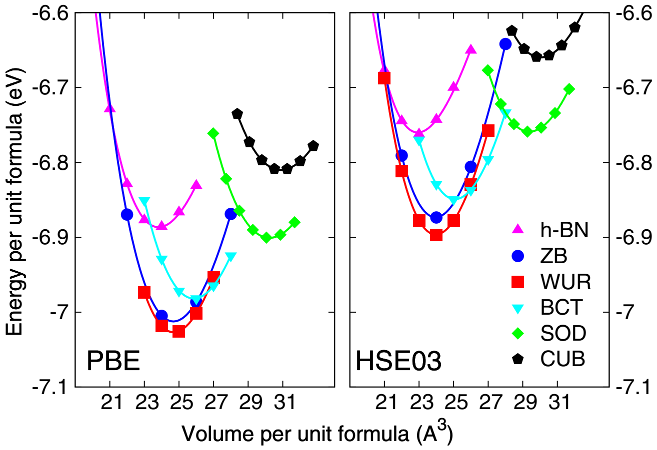

FIG. 3. (Color online) Energy versus volume $E(V)$ curves computed for the six ZnO polymorphs, with PBE (left panel) or HSE03 (right panel) XC functionals and the Zn^{12+} pseudopotential.

of such calculations [50–52]. For this reason we have paid particular attention to achieving an excellent convergence of the computational setup.

For all materials, the real axis is sampled with 100 energies and a cutoff energy of 560 eV is used to define the dimension of the self-energy operator. The number of bands included in the G_0W_0 calculation and the k-point grid (centered at Γ) are different from structure to structure and are reported in the left part of Table III. To account for the discrete k-point sampling, raw data are convoluted with a Gaussian function of width $\sigma = 0.2$ eV.

The atomic arrangements used in each calculation are the equilibrium structures obtained with the corresponding XC potential as described in the previous section.

B. Wurtzite ZnO

The top panel of Fig. 4 displays the total density of states (DOS) of ZnO wurtzite computed with the three XC approaches. For the G_0W_0 calculation, the orbital components of the site-projected local DOS (LDOS) in the VB and CB are also reported in the middle and bottom panels of the figure, respectively. Our results are in good agreement with available theoretical calculations [4,12,31,49] and with experimental photoemission spectra [53,54].

The valence region is built from electronic states with strong O $2p$ and Zn $3d$ character and displays three main structures. At the bottom of the VB, in quantitative agreement with previous calculations [4], there is a sharp, double-peaked structure (peaks D_1 and D_2) predominantly formed by Zn $3d$ states.

TABLE III. Parameters used in the G_0W_0 QP and optical spectra calculations.

	G_0W_0 corrections		RPA + G_0W_0
	No. of bands	k grid	No. of bands
h-BN	1000	$8 \times 8 \times 6$	64
Zinc blende	560	$12 \times 12 \times 12$	36
Wurtzite	1000	$8 \times 8 \times 6$	64
bct	2160	$6 \times 6 \times 8$	100
Sodalite	2880	$6 \times 6 \times 6$	230
Cubane	3840	$4 \times 4 \times 4$	300

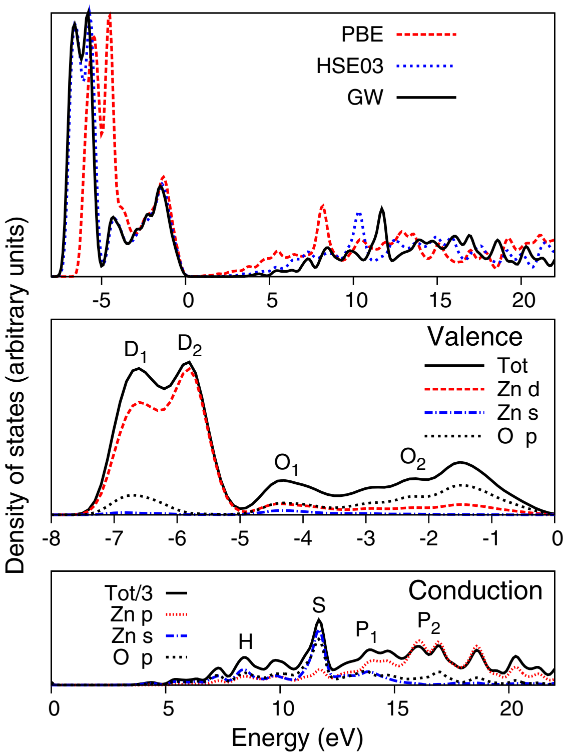

FIG. 4. (Color online) Top panel: ZnO wurtzite total DOS, calculated within PBE (red dashed), HSE03 (blue dotted), and G_0W_0 (black solid) approaches. Central panel: Atom- and orbital-projected G_0W_0 DOSs in the VB. Bottom panel: Atom- and orbital-projected G_0W_0 DOSs in the CB. All curves are aligned at the valence band maximum.

In PBE, the Zn $3d$ band extends from −6.5 to −4 eV, while it is downshifted by 1 eV in the case of HSE03 and G_0W_0 calculations, as a known result of the stronger localization of d electrons in these approaches. The d-band splitting is typical of the tetrahedral environment around Zn atoms, with a higher-energy peak D_2 of t_2 symmetry and a lower one D_1 of e symmetry. The e states are hybridized with O $2p$ states (bonding states).

At higher energies, broader structures are present, mainly formed by O $2p$ states (O_1 and O_2 regions). O_1 results from Zn $4s$−O$2p$ bonding states. In the HSE03 and G_0W_0 results, it is a well-defined peak located between −5 and −3.5 eV, whereas in PBE, it appears only as a shoulder on the Zn $3d$ LDOS which is too high in energy. The remainder of the valence band (O_2 region), extending from −3.5 eV up to the Fermi level, is mostly constituted by O$2p$−Zn$3d$ antibonding states and by hybridized O$2p$−O$2p$ states.

The lowest-energy part of the CB (from 3.31 up to ~6.6 eV in G_0W_0) is formed essentially by states of Zn $4s$ character. At around 5 eV, an additional Zn $4p$ contribution starts growing, defining region H (from 6.6 to 10.6 eV in G_0W_0). At 11.7 eV, the CB displays a sharp peak (denoted S), formed by O$2p$−Zn$4s$ antibonding states. The Zn $4p$ contribution

TABLE IV. PBE, HSE03, and G_0W_0 band gaps (eV) of the six ZnO polymorphs [55].

	E_g^{PBE}	E_g^{HSE}	$E_g^{\mathrm{G_0W_0}}$
h-BN	0.97	2.53	3.57
Zinc blende	0.63	2.13	3.18
Wurtzite	0.73	2.25	3.31
bct	0.75	2.26	3.41
Sodalite	1.05	2.43	3.63
Cubane	1.33	2.73	4.00

reaches its maximum beyond 15 eV. We denote by P_1 the region around 13.3 eV, above which Zn $4p$ states are predominant although still hybridized with Zn $4s$, and by P_2 the region around 16.0 eV, where the CB is merely formed from Zn $4p$ orbitals.

As a final remark, the use of range-separated hybrids appears especially important to obtain a correct description of valence states, while the inclusion of quasiparticle corrections (in the G_0W_0 approach) does not bring significant improvement. In contrast, G_0W_0 corrections are crucial to correctly locate the conduction band minimum, hence giving a reliable estimation of the band gap (0.73 eV in PBE, 2.25 eV in HSE03, 3.31 eV in the G_0W_0 results, to be compared to the experimental value 3.34 eV, Table IV). The CB DOS shape, on the other hand, is not significantly modified by quasiparticle corrections, which justifies the use of scissor operators or other extrapolation techniques [30], if one does not need to be quantitatively predictive of the band gap.

C. Quasiparticle spectra of ZnO polymorphs

With the view of comparing the six ZnO polymorphs, we first discuss the influence of structural parameters on the gap widths. Then the full quasiparticle spectra are analysed.

1. *Band gaps*

Table IV reports the gap widths of the six ZnO polymorphs, obtained within the PBE, HSE03, and G_0W_0 approaches. Despite the well-known overall underestimations in HSE03, which are even more severe in the PBE method, the hierarchy of gap widths in the six phases is identical within the three approaches, with a maximal gap variation (between cubane and zinc blende) of 0.7 eV in the PBE and HSE03 results and 0.8 eV in G_0W_0. This suggests that the gap hierarchy—larger gaps in less dense polymorphs—is not determined by details of the electronic structure but rather by quantities directly related to the structure. Arguments of different nature can be invoked to interpret bulk band gap variations. One refers to the strength of the electrostatic potential acting on the ions, others to hybridization effects. In the following we successively consider their applicability to ZnO band gaps.

In semiconducting or insulating compounds, the electrostatic potentials acting on anions ($V_{\mathrm{O}} > 0$) and cations ($V_{\mathrm{Zn}} < 0$) provide a contribution $\Delta V = V_{\mathrm{O}} - V_{\mathrm{Zn}} > 0$ to the atomic level separation and thus to the gap width. On the other hand, a covalent contribution to the band gap also exists, a function of the number of nearest anion-cation pairs and of their distances [56,57]. Qualitatively, ΔV is larger in denser local environments, which is well obeyed in the ZnO series when considering denser polymorphs, as seen in Fig. 5, where we report the variations of gap widths δE_g versus $\delta(\Delta V)$, with respect to E_g and ΔV in wurtzite [58]. The trends are similar in the PBE, HSE03, and G_0W_0 [59] approaches. However, the gap variations with respect to the wurtzite structure, δE_g, are much larger than those of the electrostatic potential $\delta(\Delta V)$ (0.8 eV as a whole, versus less than 0.25 eV). More importantly, the trend (decrease of E_g as ΔV increases) is actually opposite to the one expected from pure electrostatic arguments. This clearly shows that the electrostatic potential, whose contribution in ZnO polymorphs does not appear to have been previously invoked in the literature, plays a secondary role in the gap variation. Similarly, since in all (but *h*-BN) ZnO polymorphs the ions are fourfold coordinated with very similar average Zn-O distances (Table II), no significant effect of the covalent contribution is expected on δE_g.

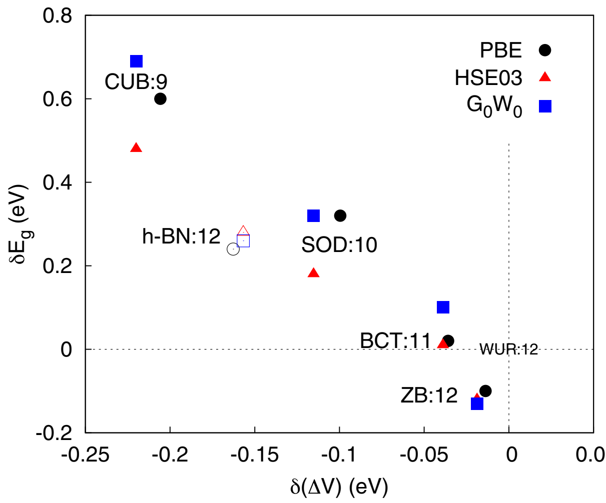

FIG. 5. (Color online) Variations of the gap widths δE_g versus the variation of electrostatic potential difference $\delta(\Delta V)$, with respect to the gap and potentials in the wurtzite structure. Results obtained within the PBE, HSE03, and G_0W_0 approximations are represented with black dots, red triangles, and blue squares, respectively. N_2 values are also reported for each structure.

As regards bandwidth effects, the states most important for fixing the gap width are those at the top of the VB and the bottom of the CB which have nearly pure O $2p$ and Zn $4s$ characters, respectively. They form bands whose width increases with the numbers of nearest O-O or Zn-Zn neighbors, i.e., N_2 [60]. As a consequence, the larger is N_2, the smaller is the gap width. Figure 5, which also indicates the values of N_2 for the various polymorphs, proves that this qualitative trend is well obeyed in all polymorphs in which atoms are tetrahedrally coordinated.

2. *Complete quasiparticle spectra*

Figure 6 reports the G_0W_0 QP spectra of all ZnO polymorphs, aligned at the VB maximum, and, aside from the *h*-BN phase, ordered from top to bottom according to decreasing

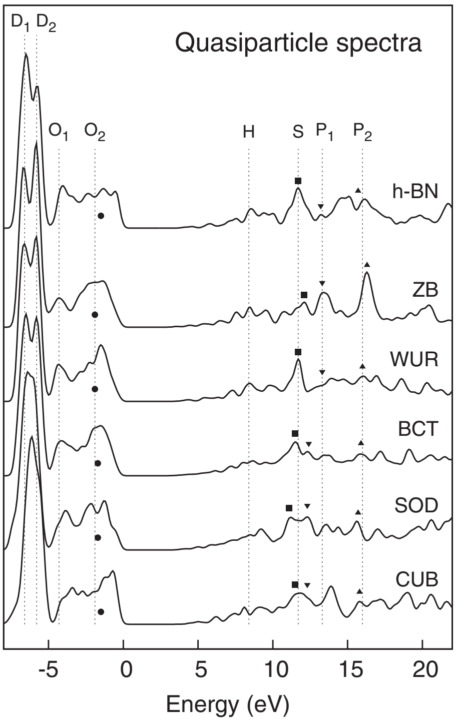

FIG. 6. G_0W_0 total density of states (arbitrary units) of the six ZnO polymorphs aligned at the top of the VB. Black round dots mark the center of gravity of the O_2 region, squares mark the position of the highest peak of Zn 4s character, and down-pointing and up-pointing triangles mark the position of the P_1 and P_2 regions respectively. Vertical lines indicate the positions of the main wurtzite structures as a guide for the eyes.

values of N_2. The DOS features discussed below follow similar trends at the PBE and HSE03 levels (not shown).

The VB of all polymorphs displays common features, such as a clear separation between the D and the O bands. The splitting of the Zn 3d levels is found in all geometries. The D_1 and D_2 peaks have pure e_g and t_{2g} characters, respectively, in zinc blende where the tetrahedral local environment is perfect. When the symmetry is progressively lowered (from wurtzite to cubane), the D_1 peak develops additional low-energy structures and is correspondingly shifted to higher energy, hence reducing the D_1-D_2 splitting. There is also a weight redistribution between D_1 to D_2, visible as well in the *h*-BN polymorph.

Higher in energy in the VB, the O_1 peak due to Zn4s−O 2p bonding states, and the O_2 region, associated with Zn 3d−O 2p antibonding states and O-O hybridization, can be recognized in all materials, although the latter displays different features from structure to structure. Nonetheless, the O_1 peak positions and the center of gravity of the O_2 region (black round dots) [61] display a systematic, albeit small, shift towards higher energy in the series (Table V), which can be assigned to the shifts of oxygen (anion) levels when V_O decreases.

The same electrostatic argument, now applied to cation levels, rationalizes the shifts of the S peak (O 2p−Zn 4s antibonding states, squares), the P_1 region (low-energy Zn 4p states, down-pointing triangles) and the P_2 region (high-energy Zn 4p states, up-pointing triangles) to lower energies in the CB, when V_{Zn} decreases in absolute value from zinc blende to cubane. In contrast to the gap which increases along the same series, the positions of the main DOS structures seem to be ruled by electrostatic arguments.

TABLE V. Position (eV) of the principal features in the G_0W_0 DOS with respect to the top of the VB

	D_1	D_2	O_1	O_2	S	P_1	P_2
h-BN	−6.4	−5.8	−4.3	−1.5	11.7	13.2	15.7
Zinc blende	−6.7	−5.8	−4.3	−1.9	12.1	13.3	16.3
Wurtzite	−6.6	−5.8	−4.3	−1.9	11.7	13.3	16.0
bct	−6.5	−5.8	−4.1	−1.7	11.5	12.4	15.9
Sodalite	−6.4	−5.9	−3.8	−1.7	11.1	12.3	15.7
Cubane	−6.1	−5.6	−3.6	−1.5	11.5	12.4	15.8

To summarize, we have evidenced systematic trends in the variations of gaps and DOSs—whether resulting from the PBE, HSE03, or G_0W_0 approximation—along the series of ZnO polymorphs. The increase of the gap widths and the evolution of the DOSs close to band edges when the number of second neighbors N_2 decreases in the ZnO series has been assigned to a narrowing of bandwidths associated with O-O hybridization and Zn-Zn hybridization at the top of the VB and bottom of CB, respectively. The lower-density polymorphs, like cubane and sodalite, thus possess the larger gaps, consistently with Ref. [30], where the authors put forward nanoporosity as a way to increase the band gap. In contrast, the shifts of the main DOS structures, towards higher energies in the VB and lower energies in the CB can be rationalized by electrostatic potential arguments, the strength (absolute value) of the electrostatic potential decreasing as the atomic density gets lower, thus pushing the oxygen and zinc atomic levels closer to each other.

IV. OPTICAL PROPERTIES

After a presentation of the computational setup, this section provides the absorption and EELS spectra first of ZnO wurtzite, and then of the other polymorphs. The discussion stresses the relationship between the optical spectra and the DOS structures.

A. Theory and methods

In linear response theory, the response of an electronic system to a perturbing field is described by the complex dielectric function $\epsilon(\mathbf{q},\omega) = \epsilon_1(\mathbf{q},\omega) + i\epsilon_2(\mathbf{q},\omega)$ where $\mathbf{q}$ is the exchanged momentum ($\mathbf{q} \to \mathbf{0}$ for light) and ω is the energy of the perturbation (photon energy in absorption or electron-energy loss in EELS). Its real and imaginary parts, which are connected by Kramers-Kronig relations, enter the expressions of the optical absorption spectrum $A_{xx}(\omega)$ (light propagating along the $\hat{x}$ direction [62]):

$$A_{xx}(\omega) = \lim_{\mathbf{q}\to 0} \epsilon_2(\mathbf{q},\omega) \quad \text{with } \mathbf{q} = q_x \tag{1}$$

and of the electron-energy loss spectrum $L(\mathbf{q},\omega)$:

$$L(\mathbf{q},\omega) = -\mathrm{Im}\left[\frac{1}{\epsilon(\mathbf{q},\omega)}\right] = \frac{\epsilon_2(\mathbf{q},\omega)}{\epsilon_1(\mathbf{q},\omega)^2 + \epsilon_2(\mathbf{q},\omega)^2}. \tag{2}$$

Structures in ϵ_2, associated with interband transitions, are directly reflected in the absorption spectra, but also in EELS when the denominator in Eq. (2) is small. Moreover, $L(\mathbf{q},\omega)$ displays additional structures (plasmon peaks) when $\epsilon_1 = 0$ and ϵ_2 is small.

In the random phase approximation [44], and under the assumption of a homogeneous medium (neglect of local fields), the dielectric function $\epsilon(\mathbf{q},\omega) = 1 - 4\pi\chi^0(\mathbf{q},\omega)/|\mathbf{q}|^2$ is expressed in terms of the macroscopic component of the independent particle polarizability $\chi^0(\mathbf{q},\omega)$, which can be computed as a weighted sum over transitions between quasiparticle states (RPA + G_0W_0) [63,64]. The knowledge of initial- and final-state energies of each transition allowed us to map them on the DOS, and to identify principal contributions by their associated weights (matrix elements).

In the present study, all spectra are computed within the RPA + G_0W_0 method [65] using the VASP code [66]. They are converged with a cutoff energy of 500 eV, and calculated for ω up to 30 eV. In the right side of Table III we report the number of bands needed for convergence of the spectra, while the **k**-point grids used are the same as for the G_0W_0 results (same table, left side). Absorption and EELS spectra are computed at momentum transfer $\mathbf{q} \approx \mathbf{0}$. For anisotropic materials, the ordinary (OCs) and extraordinary (ECs) components are given, with momentum transfer respectively parallel and perpendicular to the *ab* plane. Except when explicitly stated, local field effects are neglected. Spectra are convoluted with a Gaussian distribution of width $\sigma = 0.5$ eV to correct for the discrete sampling of the Brillouin zone.

B. Wurtzite structure

The frequency dependences of the real and imaginary parts of the dielectric function of wurtzite ZnO are shown in the top panel of Fig. 7. The wurtzite structure being anisotropic, for each of them, OCs and ECs are specified. The onset of the $\epsilon_2(\omega)$ curve is characterized by a step region, labeled E, originating from transitions between the topmost part of the VB and the Zn 4*s* states, forming the bottom of the CB. Because of the anisotropy of the wurtzite structure, the value of the absorption onset is different for the OCs and ECs (3.3 and 3.6 eV, respectively). This part of the spectrum is known to be strongly affected by excitonic effects [67,68], absent in our calculations, so it will not be further discussed.

Beyond the onset region, the main absorption peaks [in the $\epsilon_2(\omega)$ curve] occupy the energy range between ~7 and ~20 eV. This part of the spectrum is composed mostly of transitions from the upper O_2 region of the VB to the Zn 4*s* and Zn 4*p* final states. The main structures, A at 9.9 eV, B_1 and B_2 between 12.7 eV and 16.6 eV, and the C shoulder at ~17.6 eV correspond to transitions from O_2 to H, O_2 to S/P_1, and O_2 to P_2, respectively (with reference to the DOS structures, Fig. 4). Although their energies also fall in this range, transitions from the Zn 3*d* states (levels D_1 and D_2 in the DOS) have a small weight and their contributions to this part of the spectrum are negligible. In contrast, the small X steplike structures located at 21.5 and 22.1 eV in both OCs and ECs are due to transitions from D_2 to the P_2 region. Comparing our results to Refs. [67,68], in this energy range, the inclusion of electron-hole interaction redshifts all spectral features quasirigidly by about 2 eV. Hence, even without the inclusion of excitonic effects, a meaningful comparison of the absorption spectra of the six ZnO polymorphs can be made. Additionally, the comparison between RPA + G_0W_0 results with and without local fields (inset in Fig. 7) shows that the latter can be neglected as long as peak positions only are concerned.

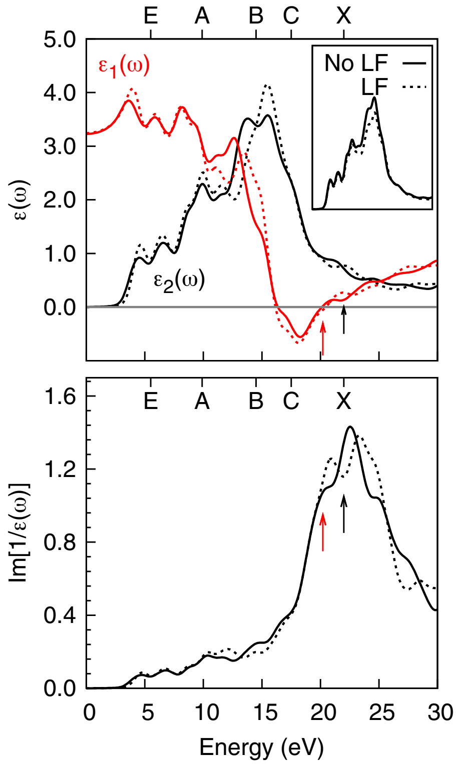

FIG. 7. (Color online) Top panel: Real (red) and imaginary (black) parts of the RPA + G_0W_0 dielectric tensor in wurtzite ZnO. OCs and ECs are reported with solid and dashed lines respectively. Inset: Absorption spectrum averaged over the three Cartesian directions, Bottom panel: EELS spectrum at vanishing parallel (solid line) and perpendicular (dashed line) momentum transfer in the RPA + G_0W_0 calculation. Red and black arrows mark the positions where the real part vanishes and has a local minimum, respectively.

The wurtzite ZnO EELS spectrum is reported in the bottom panel of Fig. 7. It displays very weak structures associated with the interband transitions E, A, B, and C. The strongest peaks in the OCs (ECs), at 20.4 (20.9) eV and 22.5 (23.3) eV, are the signatures of the plasmon resonance and of the X interband transition, respectively. The X transition is much more visible in EELS than in absorption due to the low value of the denominator in Eq. (2). As regards the plasmon resonance, as can be expected from Eq. (2), its energy is close to but not exactly equal to the energy where $\epsilon_1(\omega)$ vanishes (20.1 and 20.5 eV for the OCs and ECs, respectively).

C. Other polymorphs

The RPA + G_0W_0 absorption spectra are reported in Fig. 8 for the series of six ZnO polymorphs under consideration. As a result of the opening of the band gap, the onset moves to higher energies in the series. The anisotropic effect observed

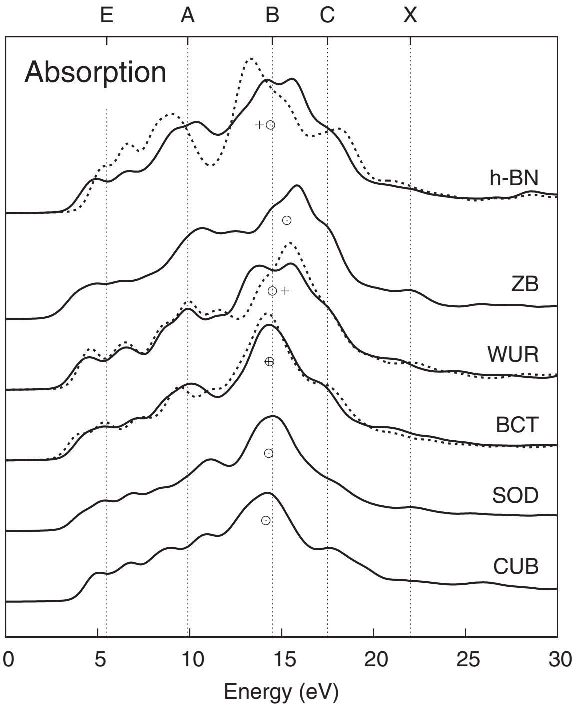

FIG. 8. Absorption spectrum of the six ZnO polymorphs. OCs and ECs are reported with solid and dashed lines, respectively. Circles and crosses indicate the position of the center of gravity of the B peak. The positions of wurtzite peaks E, A, B, C, and X are indicated by vertical lines to guide the eye.

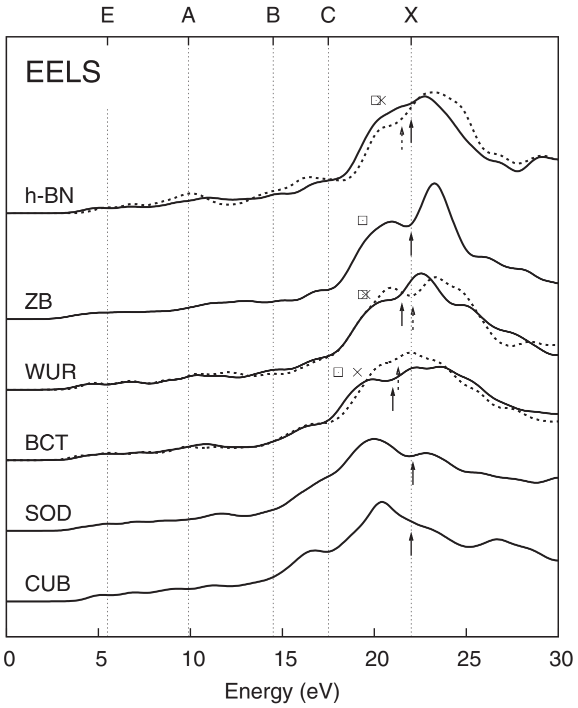

FIG. 9. EELS spectra of the six ZnO polymorphs. OCs (parallel) and ECs (perpendicular) spectra are reported with solid and dashed lines, respectively. Squares and × signs mark the energies where $\epsilon_1(\omega) = 0$ for OCs and ECs. An arrow indicates the position of the X structure. The positions of wurtzite peaks E, A, B, C, and X are indicated by vertical lines to guide the eye.

in the onset of wurtzite, can be found also in both bct [69] and the *h*-BN lattice (3.4 eV for the OCs and 3.6 eV for the EC, in the former; 3.6 eV and 4.2 eV for the latter). The E, A, B, C, and X regions can be distinguished in all spectra. As a general trend, both the E and A regions (transitions from the top of the VB to low-energy Zn 4s and Zn 4p states) are blueshifted along the series, which can be related to the increase of band gaps. The higher-energy B peak, which corresponds to transitions from the O_2 to the S and P_1 DOS regions, is strongly affected by the anisotropy of the materials. It displays a double structure only in wurtzite and zinc blende, where the final states are well separated, while, in the other polymorphs, a single broad structure appears. Unlike the E and A interband transitions, it is globally redshifted along the series, as highlighted in Fig. 8 and reported in Table VI. This trend is in agreement with the electrostatic potential effect which pushes the oxygen and zinc levels closer to each others in the series. Finally, the C and X transitions do not move significantly from structure to structure, as a result of the nearly constant energy position around 16 ± 0.3 eV of the final states (P_2 region).

TABLE VI. Positions of the B peaks (eV), zeros of $\epsilon_1(\omega)$ (eV), and electronic density n (Å^{-3}). Values for the ECs are reported in parentheses.

	B	$\epsilon_1 = 0$	$n^{1/2}$
h-BN	14.4 (13.8)	20.6 (20.8)	1.29
Zinc blende	15.3	20.3	1.26
Wurtzite	14.5 (15.2)	20.1 (20.5)	1.26
bct	14.4 (14.3)	19.1 (20.1)	1.23
Sodalite	14.3		1.14
Cubane	14.1		1.12

The EELS spectra are reported in Fig. 9. All polymorphs display a main structure around 20 eV, which progressively redshifts and broadens along the series from zinc blende to cubane. As for wurtzite, this structure involves the plasmon peak and the X interband transition. The classical model based on the free-electron gas predicts that the plasmon frequency scales as the square root of the (valence) electron density n: $\omega_p \propto \sqrt{n}$. According to it, a decrease of ω_p along the series is expected, as well as a decrease of the energy for which $\epsilon_1(\omega)$ vanishes, in agreement with numerical results (Table VI). However, ZnO is not a free-electron-gas material. This clearly appears in the mere fact that $\epsilon_1(\omega)$ never vanishes in sodalite and cubane, and shows that a more careful analysis of the frequency dependence of ϵ_1 and ϵ_2 is needed.

Due to the Kramers-Kronig relations which link $\epsilon_1(\omega)$ and $\epsilon_2(\omega)$, intense and narrow peaks in $\epsilon_2(\omega)$ are reflected in a sharp decrease of $\epsilon_1(\omega)$ at the same energy, possibly driving it to negative values. In the ZnO polymorphs, the main structure in $\epsilon_2(\omega)$ is the B peak. Its redshift in the series, noted above, is thus fully consistent with the shift of the energy at which $\epsilon_1(\omega)$ vanishes and thus of the plasmon resonance. In sodalite and cubane, however, the B peak is not intense and sharp enough to push $\epsilon_1(\omega)$ to negative values. Additionally, as visible in Fig. 10 in the case of cubane, the C shoulder, which is well detached from the B peak, induces a rise of $\epsilon_1(\omega)$, thus impeding it to vanish. Nevertheless, the two local minima of $\epsilon_1(\omega)$ are sufficiently close to zero [and $\epsilon_2(\omega)$ sufficiently

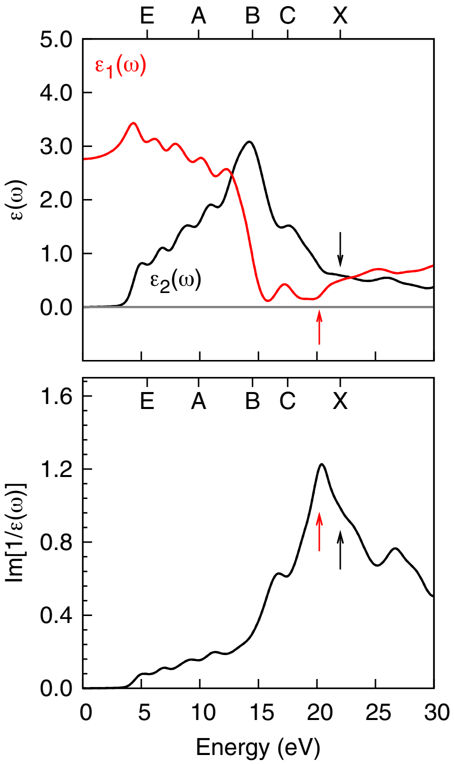

FIG. 10. (Color online) Cubane optical properties: Top panel: Real (red) and imaginary (black) parts of the dielectric tensor in RPA + G_0W_0. Bottom panel: Electron energy-loss spectrum at vanishing momentum. Red and black arrows mark the positions of the first minimum of $\epsilon_1(\omega)$ and of the X transition, respectively.

small] to generate strong peaks in the EELS, although the latter cannot be considered as genuine plasmon resonances. A similar situation occurs in sodalite.

Aside from the plasmon peaks, most spectra display an additional structure, in the same energy range, due to the X interband transition, between the D_2 states and the P_2 DOS region. In zinc blende, its intensity is high both because of the pure tetrahedral local environment of the atoms which yields a well-defined $e_g - t_{2g}$ splitting and because of the final-state localization (state at 16.3 eV in Fig. 6). Along the series from zinc blende to cubane, the intensity of the peak decreases with local symmetry lowering, due to the associated intensity loss of the initial D_2 DOS state.

To summarize, we have evidenced systematic trends in the shapes of absorption and EELS spectra, along the series of ZnO polymorphs, and we have related them to the behavior of the DOS structures discussed in the preceding section. The onset of absorption moves to higher energies in the series as a consequence of the opening of the band gap, which also induces a blueshift of the low-energy interband transitions. In contrast, the decrease of electrostatic potential along the series, which brings oxygen and zinc levels closer to each other, shifts the main absorption peak to lower energies. This provokes a decrease of the frequency at which $\epsilon_1(\omega)$ vanishes and of the plasmon resonance. The cubane and sodalite polymorphs were shown not to possess genuine plasmon resonances.

V. CONCLUSIONS

This work provides a complete characterization of the electronic properties of six ZnO polymorphs, including quasiparticle, absorption, and EELS spectra. It focuses on the series zinc blende, wurtzite, (ideal) bct, sodalite, and cubane structures, along which atoms have similar local tetrahedral environments and decreasing atomic density. The *h*-BN structure was added in view of its importance in ultrathin films. Computations rely on the PBE and HSE03 approaches for structural properties, on G_0W_0 corrections to the HSE03 eigenvalues for the simulation of QP spectra, and on the RPA + G_0W_0 method to determine the dielectric tensors and the absorption and EELS spectra.

The decrease of the atomic density along the series has two main consequences which can be traced in the electronic properties. First, due to the decrease of the number of second neighbors, a band narrowing close to the gap edge takes place. Second, the electrostatic potential acting on the oxygen and zinc ions decreases (in absolute value), pushing their atomic levels closer to each other. These effects are quite general and independent of the level of approximation chosen.

The band narrowing induces an increase of the band gap and a blueshift of the interband low energy transitions. The second effect is responsible for shifts of the main DOS structures, towards higher energies in the VB and lower energies in the CB. As a consequence, the main absorption peak, the frequency at which $\epsilon_1(\omega)$ vanishes and the plasmon resonance shift to lower energies. The cubane and sodalite polymorphs were shown not to possess genuine plasmon resonances.

This study provides a firm theoretical support to the analysis of spectroscopic experiments on ZnO polymorphs. Moreover, it gives the necessary background for forthcoming studies of ZnO nano-objects, in which, additionally, finite-size effects will need to be taken into account.

ACKNOWLEDGMENTS

We acknowledge Dr. C. Rödl for the very valuable help offered in using, understanding, and optimizing VASP calculations. This work was granted access to the HPC resources of The Institute for Scientific Computing and Simulation financed by Region Île de France and the project Equip@Meso (Reference No. ANR-10-EQPX-29-01) overseen by the French National Research Agency (ANR) as part of the "Investissements d'Avenir" program. Computations were also performed using HPC resources from GENCI-[TGCC/CINES/IDRIS] (Grant No.100170).

---

[1] R. A. Powell, W. E. Spicer, and J. C. McMenamin, Phys. Rev. B **6**, 3056 (1972).

[2] J. Muscat, A. Wander, and N. M. Harrison, Chem. Phys. Lett. **342**, 397 (2001).

[3] M. Usuda, N. Hamada, T. Kotani, and M. van Schilfgaarde, Phys. Rev. B **66**, 125101 (2002).
[4] J. Uddin and G. E. Scuseria, Phys. Rev. B **74**, 245115 (2006).
[5] M. Shishkin and G. Kresse, Phys. Rev. B **75**, 235102 (2007).
[6] A. Schleife, C. Rödl, F. Fuchs, J. Furthmüller, F. Bechstedt, P. H. Jefferson, T. D. Veal, C. F. McConville, L. F. J. Piper, A. DeMasi, K. E. Smith, H. Lösch, R. Goldhahn, C. Cobet, J. Zúñiga-Pérez, and V. Muñoz-Sanjosé, J. Korean Phys. Soc. **53**, 2811 (2008).
[7] J. A. Berger, L. Reining, and F. Sottile, Phys. Rev. B **85**, 085126 (2012).
[8] D. Waroquiers, A. Lherbier, A. Miglio, M. Stankovski, S. Poncé, M. J. T. Oliveira, M. Giantomassi, G.-M. Rignanese, and X. Gonze, Phys. Rev. B **87**, 075121 (2013).
[9] Ü. Özgür, Ya. I. Alivov, C. Liu, A. Teke, M. A. Reshchikov, S. Doğan, V. Avrutin, S.-J. Cho, and M. Morkoç, J. Appl. Phys. **98**, 041301 (2005).
[10] C. Klingshirn, Phys. Status Solidi B **244**, 3027 (2007).
[11] C. Klingshirn, J. Fallert, H. Zhou, J. Sartor, C. Thiele, F. Maier-Flaig, D. Schneider, and H. Kalt, Phys. Status Solidi B **247**, 1424 (2010).
[12] A. Schleife, F. Fuchs, J. Furthmüller, and F. Bechstedt, Phys. Rev. B **73**, 245212 (2006).
[13] J. Carrasco, F. Illas, and S. T. Bromley, Phys. Rev. Lett. **99**, 235502 (2007).
[14] J. Wang, A. J. Kulkarni, K. Sarasamak, S. Limpijumnong, F. J. Ke, and M. Zhou, Phys. Rev. B **76**, 172103 (2007).
[15] C. R. A. Catlow, S. A. French, A. A. Sokol, A. A. Al-Sunaidi, and S. M. Woodley, J. Comput. Chem. **29**, 2234 (2008).
[16] S. Zhang, Y. Zhang, S. Huang, P. Wang, and H. Tian, Chem. Phys. Lett. **557**, 102 (2013).
[17] C. H. Bates, W. B. White, and R. Roy, Science **137**, 993 (1962).
[18] T. Kogure and Y. Bando, J. Electron Microsc. **47**, 7903 (1993).
[19] A. B. M. A. Ashrafi, A. Ueta, A. Avramescu, H. Kumano, I. Suemune, Y.-W. Ok, and T.-Y. Seong, Appl. Phys. Lett. **76**, 550 (2000).
[20] S.-K. Kim, S.-Y. Jeong, and C.-R. Cho, Appl. Phys. Lett. **82**, 562 (2003).
[21] C. L. Puyeo, S. Siroky, S. Landsmann, M. W. E. van den Berg, M. R. Wagner, J. S. Reparaz, A. Hoffmann, and S. Polarz, Chem. Mater. **22**, 4263 (2010).
[22] Zhong Lin Wang, J. Phys.: Condens. Matter. **16**, R829 (2004).
[23] F. Claeyssens, C. L. Freeman, N. L. Allan, Y. Sun, M. N. R. Ashfold, and J. H. Harding, J. Mater. Chem. **15**, 139 (2005).
[24] C. L. Freeman, F. Claeyssens, N. L. Allan, and J. H. Harding, Phys. Rev. Lett. **96**, 066102 (2006).
[25] Benjamin J. Morgan, Phys. Rev. B **80**, 174105 (2009).
[26] I. Demiroglu and S. T. Bromley, Phys. Rev. Lett. **110**, 245501 (2013).
[27] J. E. Jaffe, J. A. Snyder, Z. Lin, and A. C. Hess, Phys. Rev. B **62**, 1660 (2000).
[28] J. Sun, H.-T. Wang, J. He, and Y. Tian, Phys. Rev. B **71**, 125132 (2005).
[29] W. Sangthong, J. Limtrakul, F. Illas, and S. T. Bromley, Phys. Chem. Chem. Phys. **12**, 8513 (2010).
[30] I. Demiroglu, S. Tosoni, F. Illas, and S. T. Bromley, Nanoscale **6**, 1181 (2014).
[31] D. Zagorac, J. C. Schön, J. Zagorac, and M. Jansen, Phys. Rev. B **89**, 075201 (2014).
[32] P. E. Blochl, Phys. Rev. B **50**, 17953 (1994).
[33] G. Kresse and D. Joubert, Phys. Rev. B **59**, 1758 (1999).
[34] G. Kresse and J. Furthmüller, Comput. Mater. Sci. **6**, 15 (1996).
[35] J. P. Perdew, K. Burke, and M. Ernzerhof, Phys. Rev. Lett. **77**, 3865 (1996); **78**, 1396(E) (1997).
[36] V. I. Anisimov, F. Aryasetiawan, and A. I. Lichtenstein, J. Phys.: Condens. Matter **9**, 767 (1997).
[37] F. Birch, Phys. Rev. **71**, 809 (1947).
[38] H. Karzel, W. Potzel, M. Köfferlein, W. Schiessl, M. Steiner, U. Hiller, G. M. Kalvius, D. W. Mitchell, T. P. Das, P. Blaha, K. Schwarz, and M. P. Pasternak, Phys. Rev. B **53**, 11425 (1996).
[39] S. Desgreniers, Phys. Rev. B **58**, 14102 (1998).
[40] H. Liu, Y. Ding, M. Somayazulu, J. Qian, J. Shu, D. Häusermann, and H.-K. Mao, Phys. Rev. B **71**, 212103 (2005).
[41] Deduced from experimental Zn heat of vaporization, ZnO enthalpy of formation, and O2 binding energy in *CRC Handbook of Chemistry and Physics*, 58th ed., edited by R. C. Weast (CRC, Boca Raton, FL, 1977).
[42] M. Hellström, K. Jorner, M. Bryngelsson, S. E. Huber, J. Kullgren, T. Frauenheim, and P. Broqvist, J. Phys. Chem. C **117**, 17004 (2013).
[43] L. Hedin, J. Phys.: Condens. Matter **11**, R489 (1999).
[44] G. Onida, L. Reining, and A. Rubio, Rev. Mod. Phys. **74**, 601 (2002).
[45] M. Shishkin and G. Kresse, Phys. Rev. B **74**, 035101 (2006).
[46] T. Kotani, M. van Schilfgaarde, and S. V. Faleev, Phys. Rev. B **76**, 165106 (2007).
[47] C. Friedrich, S. Blügel, and A. Schindlmayr, Phys. Rev. B **81**, 125102 (2010).
[48] J. Klimeš, M. Kaltak, and G. Kresse, Phys. Rev. B **90**, 075125 (2014).
[49] C. Rödl and A. Schleife, Phys. Status Solidi A **211**, 74 (2014).
[50] B.-C. Shih, Y. Xue, P. Zhang, M. L. Cohen, and S. G. Louie, Phys. Rev. Lett. **105**, 146401 (2010).
[51] C. Friedrich, M. C. Müller, and S. Blügel, Phys. Rev. B **83**, 081101(R) (2011).
[52] M. Stankovski, G. Antonius, D. Waroquiers, A. Miglio, H. Dixit, K. Sankaran, M. Giantomassi, X. Gonze, M. Côté, and G.-M. Rignanese, Phys. Rev. B **84**, 241201(R) (2011).
[53] L. Ley, R. A. Pollak, F. R. McFeely, S. P. Kowalczyk, and D. A. Shirley, Phys. Rev. B **9**, 600 (1974).
[54] W. Ranke, Solid State Commun. **19**, 685 (1976).
[55] All band gaps reported in Table IV were obtained with a fine k-point grid, necessary for quasiparticle calculations. As a consequence the PBE and HSE03 values are slightly improved compared to those given in Table II, obtained with a coarser k-point grid, compatible with convergence of structural characteristics only.
[56] C. Noguera, Surf. Rev. Lett. **8**, 121 (2001).
[57] C. Noguera, *Physics and Chemistry at Oxide Surfaces* (Cambridge University Press, Cambridge, 1996).
[58] Average electrostatic potentials are evaluated by locating a test charge with norm unity at each ion core, as implemented in VASP [34].
[59] The G_0W_0 wave functions are the HSE03 ones; hence the potential energy differences in HSE03 and G_0W_0 calculations are identical, although the value of the gap changes.
[60] F. Cyrot-Lackmann, J. Phys. Chem. Solids **29**, 1235 (1968).
[61] The center of gravity of the O_2 region is computed by defining its lower limit as the energy where the O 2s state contribution vanishes and its upper limit as the VB maximum.

[62] The absorption spectrum A_{ij} is in general the imaginary part of the macroscopic dielectric tensor $\epsilon_M^{ij}(\omega)$. In some anisotropic materials, off-diagonal elements A_{ij} with $i \neq j$ can be accessed by generalizations of Eq. (1).

[63] S. L. Adler, Phys. Rev. **126**, 413 (1962).

[64] N. Wiser, Phys. Rev. **129**, 62 (1963).

[65] Since G_0W_0 corrections are applied to HSE03 energies, the wave functions used to compute the random phase approximation polarizabilities are those obtained in HSE03.

[66] M. Gajdoš, K. Hummer, G. Kresse, J. Furthmüller, and F. Bechstedt, Phys. Rev. B **73**, 045112 (2006).

[67] A. Schleife, C. Rödl, F. Fuchs, J. Furthmüller, and F. Bechstedt, Phys. Rev. B **80**, 035112 (2009).

[68] P. Gori, M. Rakel, C. Cobet, W. Richter, N. Esser, A. Hoffmann, R. Del Sole, A. Cricenti, and O. Pulci, Phys. Rev. B **81**, 125207 (2010).

[69] In the distorted bct structure, slightly different absorption spectra are expected along a and b.